Revisiting the 1959 Hebgen Lake earthquake using optical image correlation; new constraints on near-field 3D ground displacement

Lucia Andreuttiova[1], James Hollingsworth[2], Pieter Vermeesch[1], Thomas Mitchell[1], Eric Bergman[3]

[1]Department of Earth Sciences, University College London, 5 Gower Place, WC1E 6BS London, UK
[2]Univ. Grenoble Alpes, Univ. Savoie Mont Blanc, CNRS, IRD, IFSTTAR, ISTerre, 38000 Grenoble, France
[3]Global Seismological Services, Golden, CO, USA

Key Points:

- Measurement of 3-dimensional surface displacement field produced by extensional dip-slip earthquake
- Application of optical image correlation to historical aerial imagery, thus expanding the window of remote geodetic observation
- Detection of previously unrecognised surface ruptures probably associated with the 1959 Hebgen Lake earthquake

Corresponding author: Lucia Andreuttiova, lucia.andreuttiova.16@ucl.ac.uk

Abstract
Surface displacement data from earthquakes are essential for characterizing the fault slip distribution with depth. The Hebgen Lake earthquake was a large normal event with a geometrically complex surface rupture, which broke across mountainous terrain. This study takes advantage of high-resolution historical stereo-imagery to measure the vertical and horizontal displacement from correlation of the orthorectified pre- and post-earthquake image mosaics. The results reveal new strike-slip surface ruptures which are possibly associated with the aftershocks from 18$^{\text{th}}$ August 1959. The kinematic role of these structures is likely related to the accommodation of internal deformation induced by the mainshock strain field. Additionally, the comparison of our results with the existing displacement data shows that the OIC-derived offsets often exceed the field measurements by >50%. We attribute this difference to the inelastic damage accommodated off the main rupture.

Plain Language Summary

This study quantifies the surface deformation created by the 1959 Hebgen Lake earthquake. To measure the displacement field we use optical image correlation (OIC). OIC compares the pixel locations in the pre-earthquake and post-earthquake image and calculates any displacement from the pixel-shift. The images cover a large area, which enabled us to find new fault ruptures that moved between 1947 and 1977. We also measured the displacement everywhere along the Red Canyon fault. Our displacement estimates are twice as large as those measured in the field. We think that this is because our values capture diffuse displacement away from the main fault, whereas the field measurements only show the localised component of displacement on the fault plane. This study aims to improve understanding of how fault ruptures distribute slip into their surroundings, which in turn has important implications for how we assess their seismic hazard.

1 Introduction

The Hebgen Lake earthquake (SW Montana, U.S) occurred on the 18$^{\text{th}}$ August (GMT) 1959 on westward dipping normal faults. This region lies within a zone of slow intracontinental extension, at the intersection between the Yellowstone volcanic system and the Intermountain Seismic Belt (Smith & Sbar, 1974; Chang et al., 2013). The Hebgen Lake earthquake was preceded by at least two events with similar magnitude that were dated at 1-3 ka and 10-14.5 ka by cosmogenic nuclide geochronology (Schwartz et al., 2009; Zreda & Noller, 1998). The 1959 event consisted of two sub-events with magnitude 7.0 and 6.3, respectively, separated by a 5-second time interval, and was followed by large aftershocks on the 18$^{\text{th}}$ and 19$^{\text{th}}$ of August (Doser, 1985). The subsidence associated with the Hebgen Lake earthquake was recorded over a broad area of approximately 1500 km^2, and more than 150 km^2 subsided by more than 3.1 m (Myers & Hamilton, 1964). Earthquake damage was widespread, but mainly focused on several SW trending normal faults (Waite & Smith, 2004) located northeast of the Hebgen reservoir.

The earthquake produced structurally complex surface ruptures with notable displacements along the Hebgen fault (HF), the Red Canyon fault (RCF), the Kirkwood fault (KF) and the West Fork fault (WFF). The faults have a cumulative rupture length of approximately 35.4 km and maximum vertical offsets of 6.1 m, 5.8 m, 0.6 m and 1.2 m, respectively (see Figure 1, Witkind et al., 1962). Despite some geometric complexity along the various fault ruptures, they generally strike 130° ± 10°, consistent with the fault plane solution from the main shock (Doser, 1985; Barrientos et al., 1989), and have 50° to 85° SW-dip (Witkind, 1964). Doser (1985) and Ryall (1962) locate the epicentre 15 km northeast of Hebgen Lake, with a depth of approximately 15-25 km. However,

uncertainty in the location, and especially the depth of the hypocenter makes it difficult to assess the spatial relationship between the source and the surface ruptures (Doser, 1985).

Previous studies measured the surface fault offset in the field (Witkind, 1964) and from an airborne LiDAR surface model (Johnson et al., 2018). The average offset measured along the Hebgen and Red Canyon fault scarps was ∼1.6 m and ∼2.3 m, and ∼2 m and ∼1.9 m (Witkind, 1964; Johnson et al., 2018, respectively). When extrapolated over a 0-15 km depth range, and assuming a fault dip of 70°, the resulting seismic moments, 2.9 x 10^{19} Nm and 1.2 x 10^{19} Nm, are approximately 50% lower than the seismologicaly-derived moment release (Doser, 1985). This implies that the slip at depth was significantly higher than at the surface. Few examples of such a marked shallow slip deficit (SSD) have been observed on surface rupturing normal earthquakes, owing to their relative paucity in terrestrial environments, compared with strike-slip and thrust events. Nevertheless, the 2016 Norcia earthquake of Central Italy (Villani et al., 2018; Walters et al., 2018) also displayed a strong SSD, despite producing an extensive, and complex, surface rupture. This contrasts with other examples of dip-slip faulting, such as surface rupturing thrust events, e.g. 1972 San Fernando, 1999 Chi Chi, or 2011 Tohoku earthquake, which all featured much larger slip at the surface than at depth. Several examples of SSD have also been reported for surface rupturing strike-slip faults (e.g., Jin & Fialko, 2021), based on inversion of satellite geodetic data. However, simplifications in the forward model, and how the geodetic data was sampled prior to inversion can both significantly overestimate the SSD (Magen et al., 2020; Marchandon et al., 2021). Distributed off-fault deformation is also known to play a significant role in accommodating co-seismic slip close to fault ruptures, producing widespread damage zones around faults (Mitchell & Faulkner, 2009; C. W. Milliner et al., 2015). Therefore, estimates of SSD based on simple elastic inversion of geodetic data, which do not account for off-fault deformation, may be in some cases too high.

In this study we use optical image correlation (OIC) of historical aerial photographs to (1) quantify the near-field surface displacement produced during the 1959 Hebgen Lake earthquake, and (2) better address the variability of slip between source depths and the surface. We take advantage of the stereo-overlap between aerial photos to resolve the vertical displacement, which is the dominant displacement component in the Hebgen Lake earthquake. This approach is especially valuable for the pre-InSAR time-period (pre 1992), for which there are no other methods for creating dense maps of ground displacement. Furthermore, while recent studies have highlighted a link between the off-fault damage and fault zone maturity (Dolan & Haravitch, 2014), rupture kinematics (C. Milliner et al., 2021), and dynamics (Jara et al., 2021), these studies are from strike-slip settings. Extending the geodetic observation of dip-slip earthquakes to the early 20th Century, allows us to expand on the number of well-characterized normal earthquake ruptures, providing a rare insight into the nature of off-fault deformation within extensional fault systems.

We develop a novel workflow that allows the retrieval of both horizontal and vertical displacements using OIC for the 1959 Hebgen Lake event. Unlike published estimates, our measurements constrain the full 3-D displacement field, while also allowing an assessment of the off-fault deformation over distances of several hundred meters from the primary fault core.

2 Methods

Optical image correlation (OIC) has become a standard method for retrieving the surface displacement field created by large strike-slip earthquakes (e.g., Michel et al., 1999; Van Puymbroeck et al., 2000; Leprince et al., 2007; Rosu et al., 2015; Zinke et al., 2019; Lauer et al., 2020; Gold et al., 2021). Optical image correlation measures co-seismic displacements from the pixel shift between pre-earthquake and post-earthquake images (Leprince

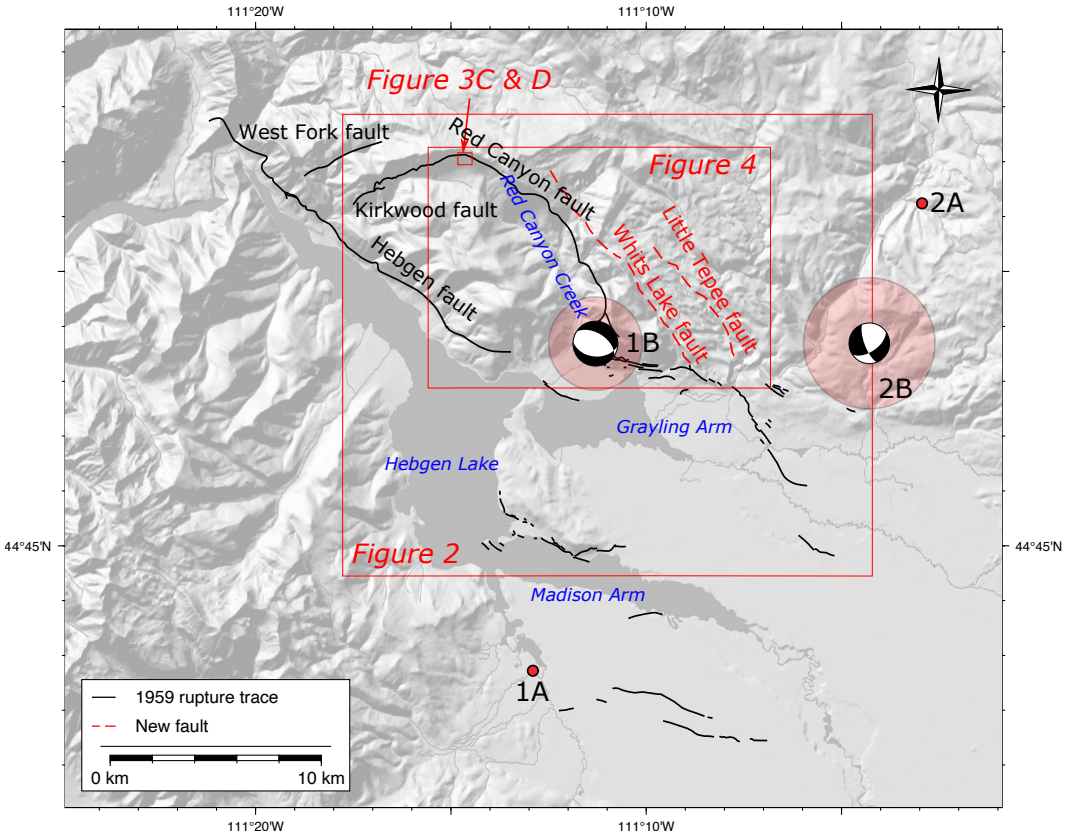

Figure 1. Overview of the earthquake area: the 1959 rupture trace mapped by the USGS (solid black line), previously unmapped faults, the Whits Lake fault and the Little Tepee fault (red dashed line), 1A and 2A are the initial locations of the main-shock and aftershock on 18/08/1959, respectively, 1B and 2B are relocated earthquakes with their respective confidence ellipses and focal mechanisms from Doser (1985). The focal mechanism for 1B (strike=95, dip=42, rake=-111) is consistent with the NW-SE trending normal faulting while 2B (strike=159, dip=71, rake=-144) appears to correlate with the left-lateral movement on the Little Tepee fault. The red rectangles highlight the areas of the all subsequent figures.

et al., 2007). The approach is optimally suited for the detection of the horizontal motion, due to the nadir view of remotely sensed optical images.

To retrieve 3-D surface displacements, we use an automatic workflow for co-registration and orthorectification of pre- and post-event aerial photographs. The workflow utilizes structure-from-motion (SfM), bundle adjustment, and stereo-matching and triangulation tools from the open-source Ames Stereo Pipeline (ASP) developed by NASA (Beyer et al., 2018). We selected pre-event stereo-images acquired on 1st July and 12th July 1947 and post-event photographs from 1st August 1977 that extend across a part of the rupture area (Figure 1). Since the historical images suffer from film distortions, scanning artifacts and image defects (Michel & Avouac, 2006; Hollingsworth et al., 2012), we built on the method described in Ajorlou et al. (2021) and Bhushan et al. (2021) and created high-resolution DEMs from the pre- and post-earthquake stereo-image pairs to precisely orthorectify aerial photographs. Precise orthorectification is crucial to remove topographic distortion and to avoid the interference of residual stereoscopic signal with the tectonic displacement in the final correlation.

We use a semi-global matching (SGM) algorithm to correlate the images. As SGM is not optimized for sub-pixel performance (Ye et al., 2020), we employ a Bayesian Expectation Maximization (Bayes EM) sub-pixel refinement (Nefian et al., 2009), which greatly reduces image noise, and gives a final precision of approximately $1/10^{\text{th}}$ pixel. The correlation algorithms compute disparity values for every pixel in the image. However, the true spatial resolution of the final correlation is limited by the size of the sub-pixel refinement correlation window (21 x 21 pixels minus the effects of a Gaussian windowing function). Hence, the combination of the SGM and Bayes EM sub-pixel refinement produces correlation maps comparable to algorithms optimized for motion tracking, while preserving a higher level of spatial detail (Leprince et al., 2007; Rosu et al., 2015). The outcome of the correlation is a pair of high-resolution maps with E-W and N-S displacements.

The horizontal displacement maps only reveal a small proportion of the displacement associated with the extensional dip-slip faulting. To characterize the 3-D displacement field, we calculate the vertical offset by subtracting the post-earthquake DEM from the pre-earthquake topography. To minimize high frequency topographic artifacts associated with differencing of laterally displaced surface, we shift the pre-earthquake DEM to the post-earthquake position. The final displacement is calculated by subtracting the pre-earthquake from the post-earthquake topography.

To mitigate the impact of the correlated noise on the final correlation we use a random forest algorithm (Breiman, 2001) to learn the relationship between correlation bias, pre- and post- image reflectance, and local topographic slope and aspect in non-deforming regions. The model is used to predict the correlation bias in regions of tectonic deformation, which is then removed (for the full details of the process see Supporting Information S1).

3 Results

Our Hebgen Lake correlations clearly reveal the normal faults known to have ruptured in the mainshock, along with two newly discovered strike-slip faults located ∼2 km east of the main surface rupture (Figure 2-b). Of the four fault scarps mapped during the original field reconnaissance (Witkind et al., 1962), only the Red Canyon Fault has displacement values significantly above the noise threshold required for meaningful structural analysis. While the Kirkwood fault and the West Fork fault are below the detection limit of the optical image correlation, the Hebgen fault has proved challenging to characterize due to its proximity to the lake, which limits the extent over which pixels can be correlated in the hanging wall. Post-seismic deformation measured by geodetic levelling after the earthquake did not exceed 32 cm (Holdahl & Dzurisin, 1991). Therefore, the deformation described in this study is largely co-seismic or related to aftershocks immediately following the earthquake. No large surface rupturing events are known from the post-earthquake period prior to acquisition of the post-event aerial images used in the analysis.

3.1 Characteristics of the Whits lake fault and the Little Tepee fault

Our correlation results reveal two previously unrecognised strike-slip faults. These structures are clearly visible in the NS displacement map (Fig. 2-b), and to a lesser extent in the EW displacements (Fig. 2-a). They are located NE of the Red Canyon fault and strike in a NW-SE direction. We refer to these new faults as the Whits Lake fault (west) and Little Tepee fault (east). Their sense of motion is primarily right-lateral and left-lateral strike-slip, respectively, with a very minor compression along the Whits Lake fault (which mutes their signal in the vertical displacement field). The median lateral offset across both faults is 2.5 m, while the median vertical separation is 0.5 m. Likely, these faults were not identified in the initial field study because of the dense vegetation

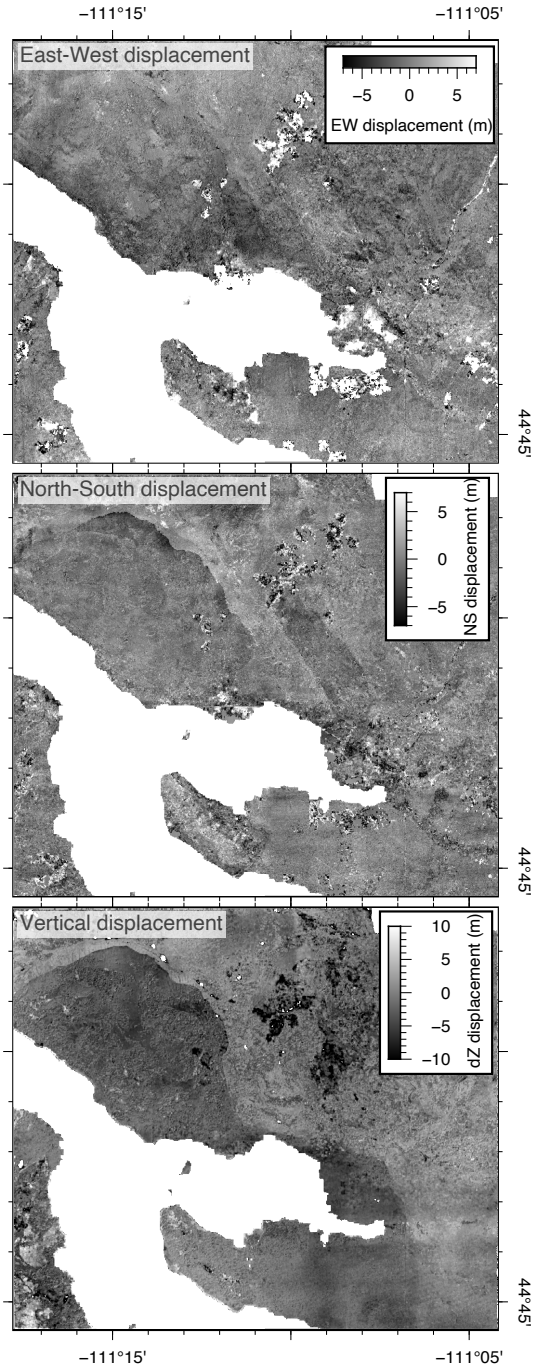

Figure 2. The correlation results show the (a) EW, (b) NS and (c) vertical displacement field from the image correlation of the pre- and post-earthquake aerial photographs and the DEM differencing. The resolution of the displacement maps is 10m/pixel. The areas of extreme values are de-correlation. (b) North South displacement component clearly shows the Lake Whits fault (west) and the Little Tepee fault (east) approximately 2 km east from the Red Canyon fault trace.

cover, the disconnected location relative to the Red Canyon and Hebgen faults, and the relatively small displacements (particularly in the vertical component).

3.2 Fault displacement measurements

From the displacement maps, we extracted 105 stacked profiles along the Red Canyon fault (stack dimensions 150×750 m). Fault-parallel, fault-perpendicular and vertical offset was calculated for each profile (for the detailed calculations of the fault offset see Supporting Information S2). We did not collect any measurements from areas of visible distributed deformation (e.g. along the SE end of the Red Canyon fault, 1 km NE of Grayling, see Fig. 1) to avoid inaccurate offset estimates. The vertical slip profile along the Kirkwood Ridge section of the RCF has an arcuate shape characteristic of normal faults (Manighetti et al., 2001) (Figure 3-a). The median vertical displacement along the RCF is ∼3.5 m, minimum ∼-4.5 m and maximum offset is ∼10 m. The horizontal component on the RCF is significantly smaller with median fault-perpendicular offset (horizontal extension) ∼2.6 m and median fault-parallel slip (strike-slip) ∼1 m (Figure S3).

We compared the fault offsets determined in this study (calculated from the vertical and fault-perpendicular components) to existing field (Witkind, 1964) and LiDAR measurements (Johnson et al., 2018) (Figure 3-a). The comparison shows a systematic overestimate of the OIC results suggesting that a large proportion of the deformation was accommodated in the rock volume surrounding the fault as permanent damage. The residual offset was calculated from the difference between the field/LiDAR data and OIC measurements. The mean of the residual offset is ±1.9 and ±1.3 m, median is ±1.5 and ±0.9 m, and maximum offset difference is ±5.3 and ±5.4 m for field and LiDAR, respectively. The percentage of off-fault deformation ranges from -35 % to 96 % for field, and -61% to 58% for the LiDAR measurements. The highest percentage of off-fault damage is recorded in the central part of the Kirkwood Ridge, approximately 3-4 km from its northwest terminus (Figure 3-b). For the LiDAR and field data we found off-fault damage magnitudes of 17±32% and 33±26%, respectively.

4 Discussion

4.1 Kinematics of the Whits Lake fault and the Little Tepee fault

Extending the analysis beyond the known earthquake area reveals reactivated surface ruptures (Whits Lake fault and Little Tepee fault) which were not associated with the 1959 Hebgen Lake mainshock. The kinematics of these faults is dextral and sinistral strike-slip, what disagrees with the NE-SW extensional deformation style for the Hebgen Lake mainshock (Waite & Smith, 2004).

However, the right-lateral motion of the Whits Lake fault coincides with the relocated focal mechanism for a M6.1 aftershock occurring at 08:41 (Doser, 1985). The original location of this event was ∼20 km to the east (Doser, 1985), however, using multiple-events hypercentroid decomposition relocation (see Supplementary Materials S5 for further details), we locate this aftershock ∼6 km east of the Whits Lake fault. While the location uncertainty for this event is ∼2 km (90% confidence), the results are still quite sensitive to details of when arrival times are used and how they are weighted. This means that each relocated aftershock could easily have an additional error of several km. Given these considerations, it is conceivable to assume that the Whits Lake fault ruptured during the 08:41 aftershock. However, due to the long time interval between the acquisition of the pre- and post-earthquake images, we are not able to associate the Whits Lake fault surface rupture with the relocated aftershocks with a 100% confidence. From the available focal mechanisms, the left-lateral motion of the Little Tepee fault appears to be consistent with the aftershock event that happened at 15:26 on 18 August 1959 (Doser, 1985) (see Fig. S5). However, the teleseismic earthquake relocations place this event ∼30 km

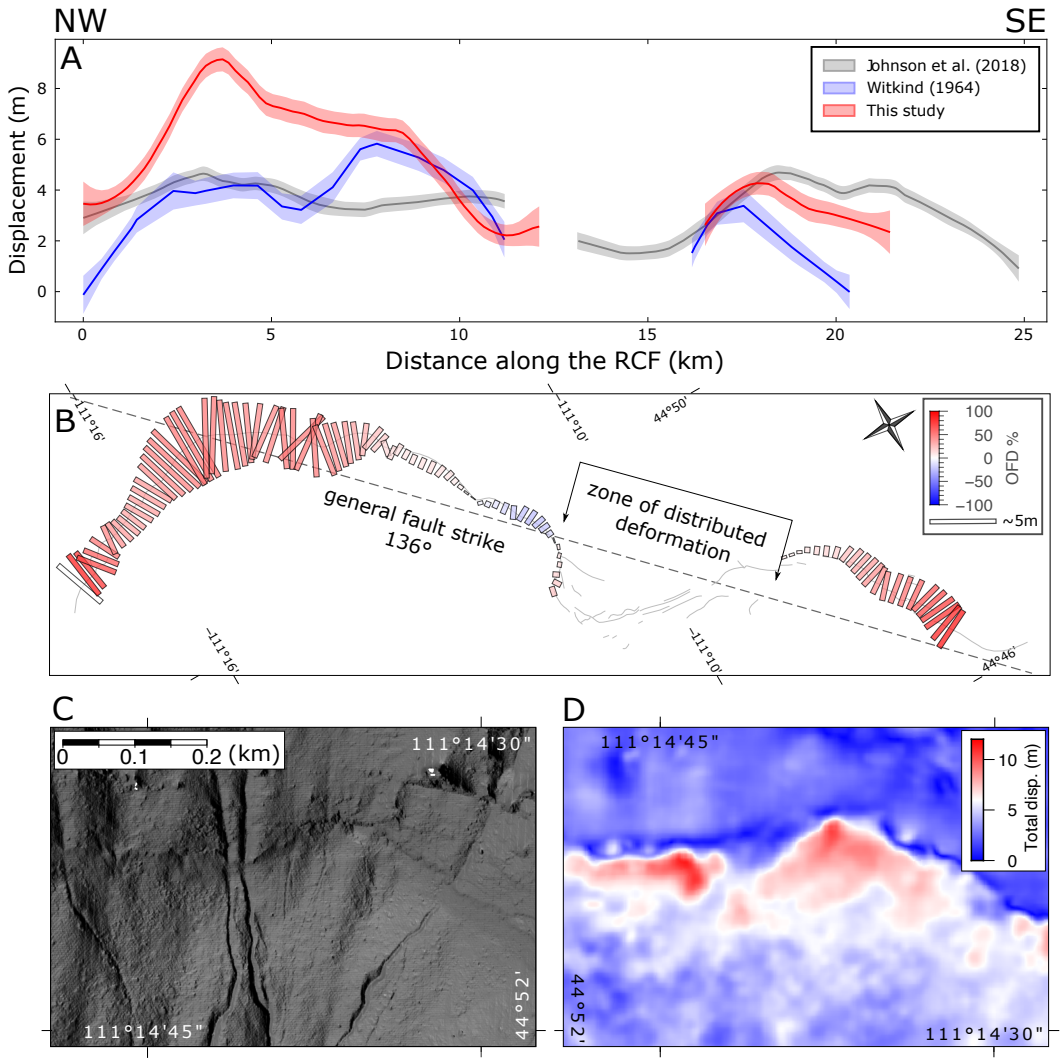

Figure 3. (a) The LOESS regression for LiDAR (Johnson et al., 2018), field (Witkind, 1964) and OIC data with the standard error of the regression model. (b) the distribution of the off-fault damage along the RCF. The color of the individual measurements represents the percentage of the off-fault deformation while the size of the bars is the relative length in m (from 0 to approximately 5 m). The pink rectangle highlights the area of distributed deformation which reflects the local deviation of the fault strike from the general strike. (c) Lidar DEM; the terrain illumination conditions are altitude/azimuth = 30°/250° , after Johnson et al. (2018). The region shown in (c) and (d) is highlighted in Figure 1.

east of the surface rupture. Such a large distance does not fall within the confidence interval. Therefore, we conclude that there is no obvious relocated aftershock that may be associated with the Little Tepee rupture.

The contrasts between the kinematics of the Whits Lake fault and Little Tepee fault and the mainshock deformation style (NE-SW extension on NW-SE faults) favors the accommodation of strain in the area. The slip vector along the Red Canyon fault rotates along-strike, while remaining approximately perpendicular to the rupture trace. If the rupture propagated unilaterally from southeast to northwest (Doser, 1985), the changing slip vector would induce a zone of extension NE of the Red Canyon fault (near 44.86°N 111.22°W) where the rupture bends from NS (north of Grayling) to EW (along Kirkwood Ridge). This zone of extension is oriented perpendicular to Kirkwood Ridge, i.e. in the NW-SE direction, and may itself be accommodated by the expulsion of a microblock to the SE, between the Whits Lake and Little Tepee faults (Figure 4). Therefore, the kinematics of these two structures likely reflects internal block deformation, induced by the changing geometry of the mainshock rupture.

The fault trace of the Whits Lake fault also coincides with a mapped geological thrust fault. Hence, it is likely that this structure represents a zone of weakness that was exploited to accommodate internal deformation around the mainshock rupture, what highlights the importance of pre-existing geological structures in accommodating present day strain.

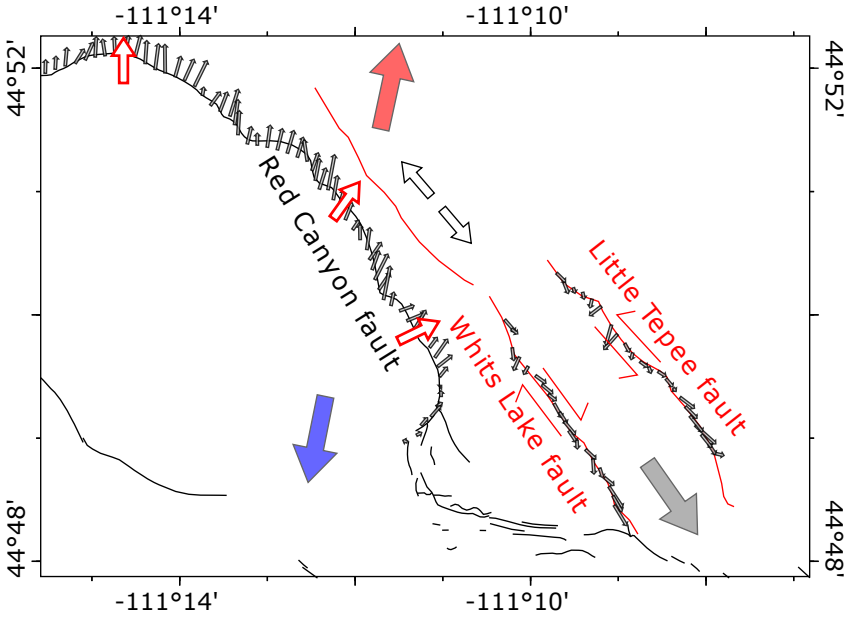

Figure 4. A map view of the Red Canyon fault, the Whits Lake fault and the Little Tepee fault (outlined in Figure 1). The large arrows show the general movement of the blocks; gray arrows show the displacement vector for each profile; white arrows show the general movement in the area and highlight the rotating vector field. Large red and blue arrows are aligned in the direction of the regional extension and represent uplift and subsidence caused by the 1959 event, respectively.

4.2 Qualitative and quantitative comparison of the OIC data with the pre-existing studies

We compare fault offsets estimated from optical correlation data with those measured in the field (Witkind, 1964), and inferred from post-event LiDAR data (Witkind, 1964). To make a meaningful comparison of our results with the values reported by Witkind (1964) and Johnson et al. (2018) (which are not sensitive to the lateral component of slip) we calculate the pure dip-slip component from the fault perpendicular and vertical offset measurements. To reduce the influence of outliers, and make a more general comparison of the first order features in each dataset, we approximate their general trends using loess regression (for OIC, LiDAR, and field, Figure 3-a). Comparison of the OIC data with the field measurements shows that, at some localities, OIC-derived offsets are up to twice as large as field and LiDAR estimates (Figure 3-b). Despite the systematically larger offset values obtained with OIC, the general trend of all data sets is comparable.

We attribute the larger offsets obtained with OIC to the off-fault damage distributed away from the fault plane. OFD represents distributed inelastic strain accommodated via secondary fracturing in the regions of increased structural complexity (e.g. fault bends) (Figure 3-c), which are more common along immature faults (Gold et al., 2015; Dolan & Haravitch, 2014). Factors such as rupture speed (Aben et al., 2020), and variable lithology (Zinke et al., 2014) also contribute to the off-fault component of slip, but to a lesser extent. Due to the distributed fracturing, the total displacement is accommodated across a wide fault zone (which extends 62.67 m, 58.5 m and 73.6 m for fault-parallel, fault-perpendicular and vertical measurements, respectively) and decays gradually away from the fault (Fig. 3-d). Since the field measurements are usually collected across a very narrow aperture that does not extend beyond the immediate proximity of the fault scarp they are not able to capture the total deformation accommodated across the wider fault zone. Similarly, Johnson et al. (2018) estimated the fault offset data from the relative height difference between the extrapolated footwall and hanging wall. While this method can capture some OFD, it is possible that a large proportion of off-fault damage remains unnoticed. On the contrary, OIC is sensitive to distributed deformation because the offset is calculated from the extrapolation through the absolute displacement values. Therefore, our OIC-derived fault offsets record the total displacement accommodated across the fault zone at the surface, comprising both on- and off-fault components.

We investigate the spatial distribution of the inelastic damage within the scope of the topographic slope, aspect, fault strike, and geological strike (Fig. S4). For a robust comparison, we used the data from the NW section of the Red Canyon fault where the fault scarp is very clear in the displacement field, and we can make high-confidence offset measurements. However, our data show no obvious correlation between the OFD distribution and the parameters listed above. Possibly, the data do not cover a large enough area to capture sufficient variation across these parameters, thereby making any comparison challenging. Nevertheless, to first order, the magnitude of off-fault deformation generally appears to increase where the fault strike deviates from the regional fault strike (e.g. given by the coseismic fault plane solution, Fig. 3-b). The deformation surrounding the Red Canyon fault could also be impacted by gravitational processes associated with the very steep topography, as well as down-dip variations in fault geometry, for which we have few constraints. Nevertheless, we do not see any local excess of slip on the fault plane, compared to the surrounding off-fault region, as was documented for the 2016 Norcia earthquake (Delorme et al., 2020), where this difference was attributed to local gravity-driven processes.

The substantially larger coseismic displacements retrieved by OIC at the surface may contribute to resolving the disparity between the seismologically-derived moment release, and the moment inferred from extrapolating surface offsets at depth. Field measurements yield moments which are 50% lower than seismological estimates (Doser, 1985).

However, if the field measurements are underestimated by up to 50%, as indicated by our data, the two moment estimates are comparable. Nevertheless, joint inversion of available geodetic data to obtain the fault slip distribution would be needed to better resolve the down-dip variability in fault slip, and better quantify the extent of SSD for the Hebgen Lake earthquake. Such an endeavor would need to take account of the complicated fault geometry, especially at depth, which will likely have a strong impact on the inversion.

5 Conclusions

In this work, we extend the application of optical image correlation to the study of historical dip-slip earthquakes, widening the window of geodetic observation to >60 years. Using a combination of optical image correlation and DEM differencing we resolve the 3-D displacement field produced by the 1959 Hebgen Lake earthquake. Due to the large ground footprint of the orthorectified image mosaics, we were able to identify previously unrecognised ruptures on the Whits Lake fault and the Little Tepee fault, which may reflect internal deformation of the surrounding region during the early postseismic period. OIC offset estimates for the Red Canyon fault are higher than the offsets measured in the field (Witkind, 1964), or inferred from post-earthquake LiDAR data (Johnson et al., 2018). We attribute this discrepancy to off-fault damage, which is not well-documented in the field or LiDAR estimates. The spatial distribution of off-fault deformation may correlate (weakly) with fault strike and geometric variability. Failure to account for off-fault damage can underestimate the total fault offset and lead to incorrect estimates of the magnitude and seismic moment from geologic data. Nevertheless, it remains unclear if the Hebgen Lake earthquake featured substantial shallow slip deficit, pending a future fault slip inversion study integrating all available geodetic data.

6 Open Research

This work uses high resolution historical aerial images that are available to download from the https://earthexplorer.usgs.gov/. The processing workflow was designed in Ames Stereo Pipeline (https://ti.arc.nasa.gov/tech/asr/groups/intelligent-robotics/ngt/stereo) (Beyer et al., 2018). The post-processing and data analysis benefited from the tools implemented in COSI-Corr (Leprince et al., 2007) and MATLAB, respectively.

Acknowledgments

LA was supported by the Natural Environment Research Council [grant number NE/L002485/1]. JH was supported by grants from BQR, Labex, and CNES. We thank Sophie Giffard-Roisin and Michel Bouchon for the helpful discussion.

References

Aben, F. M., Brantut, N., & Mitchell, T. M. (2020). Off-fault damage characterization during and after experimental quasi-static and dynamic rupture in crustal rock from laboratory p wave tomography and microstructures. *Journal of Geophysical Research: Solid Earth*, *125*(8), e2020JB019860.

Ajorlou, N., Hollingsworth, J., Mousavi, Z., Ghods, A., & Masoumi, Z. (2021). Characterizing Near-Field Surface Deformation in the 1990 Rudbar Earthquake (Iran) Using Optical Image Correlation. *Geochemistry, Geophysics, Geosystems*, *22*(6), e2021GC009704.

Barrientos, S., Stein, R., & Ward, S. (1989). Comparison of the Hebgen Lake, Montana, and the 1983 Borah Peak, Idaho, earthquakes from geodetic observations. *Bull. Seism. Soc. Am*, *79*, 2018.

Beyer, R. A., Alexandrov, O., & McMichael, S. (2018). The Ames Stereo Pipeline:

NASA's open source software for deriving and processing terrain data. *Earth and Space Science*, *5*(9), 537–548.

Bhushan, S., Shean, D., Alexandrov, O., & Henderson, S. (2021). Automated digital elevation model (DEM) generation from very-high-resolution Planet SkySat triplet stereo and video imagery. *ISPRS Journal of Photogrammetry and Remote Sensing*, *173*, 151–165.

Breiman, L. (2001). Random forests. *Machine learning*, *45*(1), 5–32.

Chang, W.-L., Smith, R. B., & Puskas, C. M. (2013). Effects of lithospheric viscoelastic relaxation on the contemporary deformation following the 1959 Mw 7.3 Hebgen Lake, Montana, earthquake and other areas of the intermountain seismic belt. *Geochemistry, Geophysics, Geosystems*, *14*(1), 1–17.

Delorme, A., Grandin, R., Klinger, Y., Pierrot-Deseilligny, M., Feuillet, N., Jacques, E., ... Morishita, Y. (2020). Complex deformation at shallow depth during the 30 october 2016 mw6. 5 norcia earthquake: interference between tectonic and gravity processes? *Tectonics*, *39*(2), e2019TC005596.

Dolan, J. F., & Haravitch, B. D. (2014). How well do surface slip measurements track slip at depth in large strike-slip earthquakes? the importance of fault structural maturity in controlling on-fault slip versus off-fault surface deformation. *Earth and Planetary Science Letters*, *388*, 38–47.

Doser, D. I. (1985). Source parameters and faulting processes of the 1959 Hebgen Lake, Montana, earthquake sequence. *Journal of Geophysical Research: Solid Earth*, *90*(B6), 4537–4555.

Gold, R. D., DuRoss, C. B., & Barnhart, W. D. (2021). Coseismic surface displacement in the 2019 ridgecrest earthquakes: Comparison of field measurements and optical image correlation results. *Geochemistry, Geophysics, Geosystems*, *22*(3), e2020GC009326.

Gold, R. D., Reitman, N. G., Briggs, R. W., Barnhart, W. D., Hayes, G. P., & Wilson, E. (2015). On-and off-fault deformation associated with the september 2013 mw 7.7 balochistan earthquake: Implications for geologic slip rate measurements. *Tectonophysics*, *660*, 65–78.

Holdahl, S. R., & Dzurisin, D. (1991). Time-dependent models of vertical deformation for the yellowstone-hebgen lake region, 1923–1987. *Journal of Geophysical Research: Solid Earth*, *96*(B2), 2465–2483.

Hollingsworth, J., Leprince, S., Ayoub, F., & Avouac, J.-P. (2012). Deformation during the 1975–1984 Krafla rifting crisis, NE Iceland, measured from historical optical imagery. *Journal of Geophysical Research: Solid Earth*, *117*(B11).

Jara, J., Bruhat, L., Thomas, M. Y., Antoine, S. L., Okubo, K., Rougier, E., ... others (2021). Signature of transition to supershear rupture speed in the coseismic off-fault damage zone. *Proceedings of the Royal Society A*, *477*(2255), 20210364.

Jin, Z., & Fialko, Y. (2021). Coseismic and early postseismic deformation due to the 2021 m7. 4 maduo (china) earthquake. *Geophysical Research Letters*, *48*(21), e2021GL095213.

Johnson, K. L., Nissen, E., & Lajoie, L. (2018). Surface rupture morphology and vertical slip distribution of the 1959 M w 7.2 Hebgen Lake (Montana) earthquake from airborne lidar topography. *Journal of Geophysical Research: Solid Earth*, *123*(9), 8229–8248.

Lauer, B., Grandin, R., & Klinger, Y. (2020). Fault geometry and slip distribution of the 2013 mw 7.7 balochistan earthquake from inversions of sar and optical data. *Journal of Geophysical Research: Solid Earth*, *125*(7), e2019JB018380.

Leprince, S., Barbot, S., Ayoub, F., & Avouac, J.-P. (2007). Automatic and precise orthorectification, coregistration, and subpixel correlation of satellite images, application to ground deformation measurements. *IEEE Transactions on Geoscience and Remote Sensing*, *45*(6), 1529–1558.

Magen, Y., Ziv, A., Inbal, A., Baer, G., & Hollingsworth, J. (2020). Fault rerupture

during the july 2019 ridgecrest earthquake pair from joint slip inversion of insar, optical imagery, and gps. *Bulletin of the Seismological Society of America*, *110*(4), 1627–1643.

Manighetti, I., King, G., Gaudemer, Y., Scholz, C., & Doubre, C. (2001). Slip accumulation and lateral propagation of active normal faults in afar. *Journal of Geophysical Research: Solid Earth*, *106*(B7), 13667–13696.

Marchandon, M., Hollingsworth, J., & Radiguet, M. (2021). Origin of the shallow slip deficit on a strike slip fault: Influence of elastic structure, topography, data coverage, and noise. *Earth and Planetary Science Letters*, *554*, 116696.

Michel, R., & Avouac, J.-P. (2006). Coseismic surface deformation from air photos: The Kickapoo step over in the 1992 Landers rupture. *Journal of Geophysical Research: Solid Earth*, *111*(B3).

Michel, R., Avouac, J.-P., & Taboury, J. (1999). Measuring ground displacements from sar amplitude images: Application to the landers earthquake. *Geophysical Research Letters*, *26*(7), 875–878.

Milliner, C., Donnellan, A., Aati, S., Avouac, J.-P., Zinke, R., Dolan, J. F., ... Bürgmann, R. (2021). Bookshelf kinematics and the effect of dilatation on fault zone inelastic deformation: Examples from optical image correlation measurements of the 2019 ridgecrest earthquake sequence. *Journal of Geophysical Research: Solid Earth*, *126*(3), e2020JB020551.

Milliner, C. W., Dolan, J. F., Hollingsworth, J., Leprince, S., Ayoub, F., & Sammis, C. G. (2015). Quantifying near-field and off-fault deformation patterns of the 1992 Mw 7.3 L anders earthquake. *Geochemistry, Geophysics, Geosystems*, *16*(5), 1577–1598.

Mitchell, T., & Faulkner, D. (2009). The nature and origin of off-fault damage surrounding strike-slip fault zones with a wide range of displacements: A field study from the atacama fault system, northern chile. *Journal of Structural Geology*, *31*(8), 802–816.

Myers, W. B., & Hamilton, W. (1964). Deformation accompanying the Hebgen Lake earthquake of August 17, 1959.

Nefian, A. V., Husmann, K., Broxton, M., To, V., Lundy, M., & Hancher, M. D. (2009). A Bayesian formulation for sub-pixel refinement in stereo orbital imagery. In *2009 16th ieee international conference on image processing (icip)* (pp. 2361–2364).

Rosu, A.-M., Pierrot-Deseilligny, M., Delorme, A., Binet, R., & Klinger, Y. (2015). Measurement of ground displacement from optical satellite image correlation using the free open-source software micmac. *ISPRS Journal of Photogrammetry and Remote Sensing*, *100*, 48–59.

Ryall, A. (1962). The Hebgen Lake, Montana, earthquake of August 18, 1959: P waves. *Bulletin of the Seismological Society of America*, *52*(2), 235–271.

Schwartz, D., Hecker, S., Stenner, H., Haller, K. M., Pierce, K. L., Lageson, D. R., & Machette, M. (2009). The 1959 Hebgen Lake, Montana, surface rupture and record of late-Pleistocene-Holocene earthquakes. In *Bulletin geological society of america annual meeting* (Vol. 41, p. 53).

Smith, R. B., & Sbar, M. L. (1974). Contemporary tectonics and seismicity of the western United States with emphasis on the Intermountain Seismic Belt. *Geological Society of America Bulletin*, *85*(8), 1205–1218.

Van Puymbroeck, N., Michel, R., Binet, R., Avouac, J.-P., & Taboury, J. (2000). Measuring earthquakes from optical satellite images. *Applied Optics*, *39*(20), 3486–3494.

Villani, F., Pucci, S., Civico, R., De Martini, P. M., Cinti, F. R., & Pantosti, D. (2018). Surface faulting of the 30 october 2016 mw 6.5 central italy earthquake: Detailed analysis of a complex coseismic rupture. *Tectonics*, *37*(10), 3378–3410.

Waite, G. P., & Smith, R. B. (2004). Seismotectonics and stress field of the Yel-

lowstone volcanic plateau from earthquake first-motions and other indicators. *Journal of Geophysical Research: Solid Earth*, *109*(B2).

Walters, R. J., Gregory, L. C., Wedmore, L. N., Craig, T. J., McCaffrey, K., Wilkinson, M., ... others (2018). Dual control of fault intersections on stop-start rupture in the 2016 central italy seismic sequence. *Earth and Planetary Science Letters*, *500*, 1–14.

Witkind, I. J. (1964). *Reactivated faults north of Hebgen Lake*. US Government Printing Office.

Witkind, I. J., Myers, W. B., Hadley, J. B., Hamilton, W., & Fraser, G. D. (1962). Geologic features of the earthquake at Hebgen Lake, Montana, August 17, 1959. *Bulletin of the Seismological Society of America*, *52*(2), 163–180.

Ye, Z., Xu, Y., Chen, H., Zhu, J., Tong, X., & Stilla, U. (2020). Area-based dense image matching with subpixel accuracy for remote sensing applications: Practical analysis and comparative study. *Remote Sensing*, *12*(4), 696.

Zinke, R., Hollingsworth, J., & Dolan, J. F. (2014). Surface slip and off-fault deformation patterns in the 2013 mw 7.7 b alochistan, p akistan earthquake: Implications for controls on the distribution of near-surface coseismic slip. *Geochemistry, Geophysics, Geosystems*, *15*(12), 5034–5050.

Zinke, R., Hollingsworth, J., Dolan, J. F., & Van Dissen, R. (2019). Three-dimensional surface deformation in the 2016 mw 7.8 kaikōura, new zealand, earthquake from optical image correlation: Implications for strain localization and long-term evolution of the pacific-australian plate boundary. *Geochemistry, Geophysics, Geosystems*, *20*(3), 1609–1628.

Zreda, M., & Noller, J. S. (1998). Ages of prehistoric earthquakes revealed by cosmogenic chlorine-36 in a bedrock fault scarp at Hebgen Lake. *Science*, *282*(5391), 1097–1099.